Examination of Phencyclidine Hydrochloride via Cryogenic Terahertz Spectroscopy, Solid-State Density Functional Theory, and X-ray Diffraction

Patrick M. Hakey, Matthew R. Hudson, Damian G. Allis, Wayne Ouellette, and Timothy M. Korter*

Department of Chemistry, Syracuse University, Syracuse, New York 13244-4100

Received: July 24, 2009; Revised Manuscript Received: September 18, 2009

The terahertz (THz) spectrum of phencyclidine hydrochloride from 7.0 to 100.0 cm^{-1} has been measured at cryogenic (78.4 K) temperature. The complete structural analysis and vibrational assignment of the compound have been performed employing solid-state density functional theory utilizing eight generalized gradient approximation density functionals and both solid-state and isolated-molecule methods. The structural results and the simulated spectra display the substantial improvement obtained by using solid-state simulations to accurately assign and interpret solid-state THz spectra. A complete assignment of the spectral features in the measured THz spectrum has been completed at a VWN-BP/DNP level of theory, with the VWN-BP density functional providing the best-fit solid-state simulation of the experimentally observed spectrum. The cryogenic THz spectrum contains eight spectral features that, at the VWN-BP/DNP level, consist of 15 infrared-active vibrational modes. Of the calculated modes, external crystal vibrations are predicted to account for 42% of the total spectral intensity.

I. Introduction

Terahertz (THz, far-infrared, <200 cm^{-1}) vibrational spectroscopy is being used for a number of important analytical applications in such areas as threat detection[1–3] and pharmaceutical characterization.[4,5] Its utility stems from solid-state compounds and molecules containing low-energy vibrations that, taken as a whole in this region, serve as spectral "fingerprints" usable for their identification, detection, and characterization. In all cases, the use of these fingerprints is dependent upon the level of confidence that exists in the understanding of the molecular origins of the spectral features. The identification of these motions plays a key role in properly interpreting the features present in experimental spectra, making absorption feature assignments a critical step in the rational use of THz spectroscopy in all analytical applications.

While there is a significant body of literature on the THz spectroscopy of pharmaceuticals, there has been relatively little work performed on the use of THz spectroscopy for the detection and identification of concealed illicit drugs.[6–8] The arylcyclohexylamine 1-(phenylcyclohexyl)-piperidine hydrochloride ($C_{17}H_{26}N \cdot Cl$, generally referred to as phencyclidine hydrochloride (PCP•HCl)) is more readily recognized by the street monikers PCP, angel dust, and hog, among others. The compound was originally developed as an anesthetic but, due to adverse effects in humans, its legal use has been limited to the veterinary realm only. The compound has been classified as a schedule II controlled substance in the United States since the 1970s.[9] The presented examination of PCP•HCl includes the experimental THz spectra (0.2−3.0 THz, 7.0−100.0 cm^{-1}) at room (293 K) and liquid-nitrogen (78.4 K) temperatures. Additionally, a complete first-principles analysis and assignment of the cryogenic spectrum using solid-state density functional theory (DFT) is presented.

II. Methods

Experimental Procedures. Experimental spectra were recorded using a pulsed time-domain THz spectrometer. Optical rectification is used to generate THz radiation, and free-space electro-optic sampling (FSEOS) is employed to detect the generated THz pulses.

A regeneratively amplified mode-locked Ti:sapphire (Ti:S) laser system comprised of four components is the foundation of the THz-TDS instrument. A diode-pumped solid-state (Nd:YVO$_4$) laser (Coherent, Verdi-5) is used to pump a Ti:S oscillator (Coherent, Mira-SPO), which seeds a Ti:S regenerative amplifier (Positive Light, Legend-HE-USP). A second diode-pumped solid-state (Nd:YLF) laser (Positive Light, Evolution-30) serves to pump the regenerative amplifier. Overall, this system delivers ultrashort pulses at a 1 kHz repetition rate with a duration of ≤40 fs and energy of ~2.5 mJ centered at λ = 800 nm. The near-infrared (NIR) pulses then propagate through a 0.5 mm zinc telluride generator crystal, creating the THz radiation via the second-order nonlinear optical process of optical rectification.[10,11] Ultimately, this system generates THz pulses with a bandwidth of 7.0−100.0 cm^{-1} and duration of ~200 fs. Any residual NIR radiation is eliminated by the presence of a poly(tetrafluoroethylene) (PTFE) disk directly behind the generator crystal. The THz radiation is directed and focused toward the sample by a pair of off-axis parabolic mirrors.

The sample is held in an evacuated variable-temperature cryostat (Janis Research Systems) to allow for temperature studies. The cryostat windows are composed of poly(methylpentene) (3 mm) because of its low absorbance of THz radiation and high rigidity. In the studies presented here, the cryostat is maintained at 293 and 78.4 K, corresponding to room temperature (RT) and liquid-nitrogen temperatures, respectively. To negate the effects of ambient water vapor, the entire path of the THz pulses is purged with dry air.

After interacting with the sample pellet, the transmitted THz radiation is focused onto a second ZnTe crystal (0.5 mm) by a

---

* Corresponding author. E-mail: tmkorter@syr.edu.

10.1021/jp907083u CCC: $40.75

second pair of off-axis parabolic mirrors. This crystal serves as the detector in the FSEOS method,[12] where the THz pulses induce a birefringence within the ZnTe crystal that is directly proportional to the amplitude and phase of the electric field of the THz pulse. The induced birefringence is measured by monitoring the amount of polarization rotation in a NIR gate pulse that spatially and temporally overlaps the THz pulse in the ZnTe crystal. A Wallaston prism and a balanced photoreceiver (New Focus 2307) are used with a lock-in amplifier (Stanford SR-830) to monitor the polarization of the NIR gate pulse. The amplifier is locked to an optical chopper (Digirad C-980) inserted into the THz generation arm and itself is synchronized to a subharmonic of the laser-repetition rate. A linear delay stage (Newport ILS150CCHA) is used to vary the arrival time of the THz pulses relative to the NIR pulses at the detector, yielding the time-domain THz waveform. The Fourier transform of this time-domain signal results in a frequency-domain transmission spectrum of the sample of interest.

The material used in this investigation was purchased from Sigma-Aldrich (≥ 98% pure by thin layer chromatography) and was used as received without additional purification. The PCP·HCl sample was pulverized using a mortar and pestle to minimize particle size, limiting the possibility of radiation scattering. After being crushed to a fine powder, the sample material was homogeneously dispersed throughout a PTFE matrix by gentle stirring. The ratio of PTFE to sample was approximately 53:1. The mixture was then pressed into a pellet 1.6 mm thick and weighing 0.51 g. PTFE is used for the filler material because of its relative transparency in the THz region. Although THz absorptions are present in pure PTFE (particularly noticeable at low temperature),[13,14] these absorptions are negated by ratioing the Fourier transformed power spectrum of a pure PTFE blank against the Fourier transformed power spectrum of the sample pellet.

The THz radiation passing through the sample pellet is averaged a total of 32 times for each individual scan. The averaged waveform data are Fourier transformed to provide a frequency power spectrum, which is then ratioed against a frequency power spectrum created from a PTFE blank. The waveform data were uncorrected for any additional potential losses.[15] The ratioing of the power spectra yields a THz absorption spectrum in the frequency range of 7.0−100.0 cm^{-1} with an instrument resolution of ∼1.5 cm^{-1}. The final cryogenic experimental THz spectrum presented here is an average of four such acquisitions measured consecutively, while the room temperature experimental data are an average of two acquisitions.

X-ray Crystallography. X-ray measurements were performed on a Bruker-AXS SMART-CCD diffractometer at low temperature (90 K) using graphite-monochromated Mo Kα radiation ($\lambda_{\text{MoK}\alpha} = 0.71073$ Å).[16] The data were corrected for Lorentz and polarization effects and absorption using SADABS.[17] The structures were solved by direct methods. All non-hydrogen atoms were refined anistropically. After all of the non-hydrogen atoms were located, the model was refined against F^2, initially using isotropic and later anisotropic thermal displacement parameters. Hydrogen atoms were introduced in calculated positions and refined isotropically. Neutral atom scattering coefficients and anomalous dispersion corrections were taken from the International Tables, Vol. C.[18] All calculations were performed using the SHELXTL crystallographic software packages.[19,20] Crystallographic details have been summarized in Table 1. No phase change is observed between 293 K ($P2(1)/c$, $a = 8.888(1)$ Å, $b = 14.132(10)$ Å, $c = 13.396(10)$ Å, $\alpha = \gamma = 90.0°$, $\beta = 104.47(17)°$, $Z = 4$)[21] and 90 K ($P2(1)/c$, $a = 8.7668(5)$ Å, $b = 13.7455(8)$ Å, $c = 13.0292(8)$ Å, $\alpha = \gamma = 90.0°$, $\beta = 103.898(2)°$, $Z = 4$). Atomic positional parameters, full tables of bond lengths and angles, and anisotropic temperature factors are available as Supporting Information.

TABLE 1: Crystal Data and Structure Refinement for PCP·HCl

identification code	p21c
empirical formula	C_{17} H_{26} Cl N
formula weight	279.84 amu
temperature	90(2) K
wavelength	0.71073 Å
crystal system	monoclinic
space group	$P2(1)/c$
unit cell dimensions	$a = 8.7668(5)$ Å $b = 13.7455(8)$ Å $c = 13.0292(8)$ Å $\alpha = 90°$ $\beta = 103.898(2)°$ $\gamma = 90°$
volume	1524.11(16) Å^3
Z	4
density (calculated)	1.220 Mg/m^3
absorption coefficient	0.239 mm^{-1}
$F(000)$	608
crystal size	0.16 × 0.10 × 0.10 mm^3
θ range for data collection	2.19−28.07°
index ranges	$-11 \leq h \leq 11$, $-18 \leq k \leq 18$, $-17 \leq l \leq 17$
reflections collected	15616
independent reflections	3710 [R(int) = 0.0726]
completeness to $\Theta = 28.07°$	99.9 %
absorption correction	multiscan
max and min transmission	0.9765 and 0.9628
refinement method	full-matrix least squares on F^2
data/restraints/parameters	3710/0/276
goodness-of-fit on F^2	1.041
final R indices [$I > 2\sigma(I)$]	R1 = 0.0547, wR2 = 0.1091
R indices (all data)	R1 = 0.0785, wR2 = 0.1199
largest diff. peak and hole	0.398 and −0.235 $\text{e}\cdot\text{Å}^{-3}$

Theoretical Procedures. Density functional theory (DFT) geometry optimizations and normal mode analyses within the harmonic approximation were performed for both solid-state PCP·HCl (using the 90 K diffraction results) and the protonated form of the phencyclidine isolated molecule ($\text{PCP}\cdot\text{H}^+$) with the DMol^3 (version 4.2)[22,23] software package. All calculations employed the DNP (double numerical with d and p polarization) basis set (comparable to a 6-31G(d,p) Gaussian-type basis set), program option "fine" grid size (corresponding to a k-point separation of 0.04 Å^{-1}), and a convergence criterion of $\Delta E < 5 \times 10^{-7}$ hartree.[22] All eight generalized gradient approximation (GGA) density functionals offered in DMol^3 were used for comparative purposes, including the BLYP,[24,25] BOP,[26] PW91,[27] HCTH,[28] BP,[24,29] PBE,[30,31] RPBE,[32] and VWN-BP[24,29,33] density functionals. As the DNP basis set is used in all cases and the optimization parameters are identical, the presented calculations are referred to simply by their functional abbreviation. DMol^3 differs from other solid-state DFT packages in that it does not optimize lattice constants, meaning the molecules within the unit cell have been optimized within the cell parameters defined by the 90 K X-ray diffraction study included in this investigation.

The solid-state infrared (IR) intensities are calculated by the difference-dipole method for each IR-active mode. These intensities are defined as the square of the change in dipole moment for the unit cell that results from atomic displacements along each normal mode coordinate ($d\mu/dq$) using the charges obtained from Mulliken population analyses, thereby considering only the IR intensity dependence on the change in dipole moment to estimate the actual intensity.[34–37]

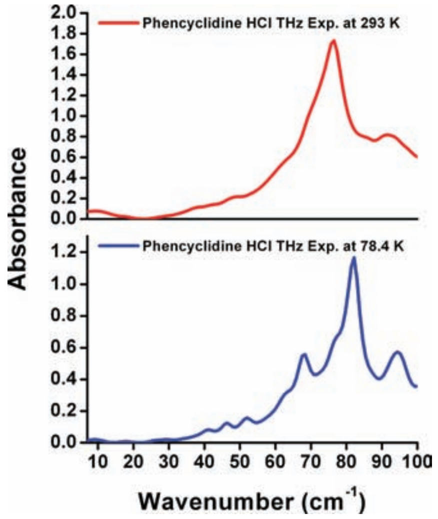

Figure 1. Experimental THz spectra of PCP·HCl at room temperature (293 K) and liquid nitrogen temperature (78.4 K).

III. Results

Experimental Procedure. The 293 and 78.4 K THz spectra of PCP·HCl from 7.0 to 100.0 cm^{-1} are shown in Figure 1. The RT spectrum contains two distinct features at 76.5 and 91.1 cm^{-1} (which correlate to the prominent features at 82.2 and 94.4 cm^{-1} in the cryogenic spectrum) and multiple weak absorptions at lower energy that are not defined well enough to be reasonably correlated to features in the cryogenic spectrum. Discernible features present in the RT spectrum are shifted to slightly higher energy in the cryogenic spectrum, with this shifting expected due to contraction of the lattice constants upon cooling.

The cryogenic THz spectrum of PCP·HCl contains several more discernible features than the RT measurement (Figure 1). As has been shown previously, cryogenic cooling is an invaluable means for gauging the accuracy of DFT spectral predictions by sharpening, and uncovering, features contained in experimental THz spectra that are not resolvable at higher temperatures.[38–40] Six peaks and two pronounced shoulders are noted in the cryogenic spectrum, leading to a total of eight assignable features in the 7−100 cm^{-1} experimental range. The six peak absorptions occur at 41.1, 46.4, 52.1, 67.9, 82.2, and 94.4 cm^{-1}. The two shoulder features were determined by Lorentzian deconvolution to occur at 62.8 and 77.5 cm^{-1}. While similar in appearance, the intensity of the feature at 94.4 cm^{-1} may be weaker than that of the feature at 67.9 cm^{-1} because of a slightly rising baseline in the spectrum. The three low-energy absorption features all display similarly weak intensities and are clustered with a similar gap in energy between each feature. Experimental spectra presented in this study have been offset to place the minimum absorbance in the measured range of the spectrum at zero.

Theoretical Procedures. ***a. Comparison of Experimental and Simulated Molecular Structures.*** Calculated structural data for PCP·HCl and PCP·H$^+$ are provided along with single crystal X-ray diffraction data in Table 2 (bond lengths) and Table 3 (bond angles). The labeling scheme for phencyclidine is provided in Figure 2. The protonated form of the phencyclidine molecule is used for the isolated-molecule calculation for consistency with the form found in the solid. In order to more easily highlight the structural differences between the solid-state and isolated-molecule calculations, Figure 3 has been included to graphically depict the deviations in the calculated bond lengths from the experimentally obtained values. The figure shows an improved agreement between theory and experiment over the isolated-molecule calculations in the solid-state calculated geometries. Also clear in Figure 3 is the trend of overestimation of the bond lengths by both the solid-state and isolated-molecule calculations.

The bond length agreement between theory and experiment is best for the PW91 and VWN-BP functionals, followed closely by the PBE and BP functionals by root-mean-square deviation (RMSD) comparison. The HCTH functional has been seen in numerous previous studies to be an excellent performer for bond length prediction in the solid state[34,35] but is found to be the fifth-best performer based upon RMSD comparisons for PCP·HCl. On comparison of the isolated-molecule optimized geometries to experiment, the results are noticeably different. The RMSD values for all eight functionals in the gas phase are substantially higher, and the geometry is best replicated by the HCTH functional based upon RMSD comparisons. The PBE and PW91 functionals follow closely behind HCTH as the second-best performers by RMSD comparison. The solid-state and isolated-molecule optimizations are least accurate in their reproductions of the C_1-N_1 bond lengths, overestimated by the solid-state calculations by an average of 0.0204 Å and overestimated by the isolated-molecule calculations by an average of 0.0680 Å. The C_1-N_1 bond length is best estimated in both methodologies by the PW91 density functional. Noticeable changes to N_1-C_n bond lengths in the solid state are to be expected due to the presence of the Cl$^-$ counterion, the resulting 0.2−0.4 Å elongation of the N−H$^+$ bond across all functionals due to the N−H$^+$·Cl$^-$ ionic interaction, and crystal packing of the three six-member rings. The average calculated distance between the proton and the Cl$^-$ ion is 2.0148 Å, an underestimation of nearly 0.13 Å when compared to the experimental data. This deviation is likely strongly tied to the uncertainty in the proton position as determined by the X-ray diffraction experiment and is, therefore, not used as a proper metric of agreement between theory and experiment. The distance from the nitrogen atom to the Cl$^-$ ion has been determined to be an average of 3.0795 Å, which is within 0.002 Å of the experimentally determined bond length. This proper comparison of heavy atom positions between theory and experiment indicates that this interatomic separation has been very well predicted by the calculations.

Bond angle agreement between theory and experiment has also been considered by RMSD comparison. Among the solid-state calculations, the PW91 optimization produces the smallest RMSD of the eight GGA functionals, followed by the BP and PBE functionals. Following very closely behind BP and PBE is the VWN-BP functional. The comparison of the predicted bond angles to the experimental values for the isolated-molecule calculations provides similar trends to those of the solid state for the best performers. The PW91 functional again provides the lowest RMSD value, with the PBE functional maintaining the second-best value. The BP and VWN-BP functional pair provide the third-best RMSD values.

In the replication of the bond angles in both the solid state and the isolated molecule, the PW91 functional produces the best simulation by RMSD comparison. It is also interesting to note that the HCTH-based calculations produce the worst RMSD values for both the solid-state and isolated-molecule predictions. In the case of the solid-state optimizations, the RMSD value for the HCTH bond angles is almost 50% larger than the next-highest RMSD value (BOP).

Bond angle agreement is not greatly improved for the solid-state calculations relative to the isolated-molecule optimizations;

TABLE 2: [Functional]/DNP Solid State ($PCP\cdot HCl$) and Isolated Molecule ($PCP\cdot H^+$) Bond Lengths (Å) and RMSD Values[a]

bond	exp	BLYP	BOP	BP	HCTH	PBE	PW91	RPBE	VWN-BP
					Solid State				
C_1-C_2	1.539	1.5518	1.5533	1.5434	1.5345	1.5438	1.5422	1.5513	1.5431
C_2-C_3	1.531	1.5410	1.5419	1.5319	1.5217	1.5317	1.5307	1.5379	1.5315
C_3-C_4	1.524	1.5325	1.5333	1.5251	1.5117	1.5249	1.5237	1.5304	1.5248
C_4-C_5	1.521	1.5332	1.5342	1.5261	1.5135	1.5262	1.5248	1.5321	1.5259
C_5-C_6	1.533	1.5425	1.5432	1.5334	1.5224	1.5329	1.5323	1.5390	1.5331
C_6-C_1	1.540	1.5544	1.5559	1.5456	1.5362	1.5462	1.5446	1.5536	1.5453
C_1-N_1	1.560	1.5984	1.5996	1.5729	1.5719	1.5719	1.5718	1.5844	1.5726
N_1-C_7	1.506	1.5183	1.5188	1.5049	1.4930	1.5044	1.5038	1.5117	1.5047
C_7-C_8	1.520	1.5274	1.5281	1.5205	1.5095	1.5206	1.5194	1.5261	1.5202
C_8-C_9	1.522	1.5313	1.5316	1.5235	1.5117	1.5232	1.5223	1.5282	1.5232
C_9-C_{10}	1.517	1.5318	1.5329	1.5245	1.5117	1.5243	1.5233	1.5299	1.5242
$C_{10}-C_{11}$	1.520	1.5287	1.5297	1.5213	1.5098	1.5211	1.5201	1.5270	1.5210
$C_{11}-N_1$	1.512	1.5221	1.5227	1.5083	1.4966	1.5077	1.5069	1.5154	1.5081
C_1-C_{12}	1.536	1.5382	1.5396	1.5317	1.5256	1.5325	1.5309	1.5386	1.5313
$C_{12}-C_{13}$	1.398	1.4085	1.4098	1.4051	1.3958	1.4054	1.4040	1.4096	1.4049
$C_{13}-C_{14}$	1.393	1.4003	1.4015	1.3984	1.3873	1.3994	1.3975	1.4039	1.3982
$C_{14}-C_{15}$	1.384	1.3951	1.3963	1.3932	1.3840	1.3940	1.3922	1.3975	1.3930
$C_{15}-C_{16}$	1.378	1.3968	1.3972	1.3939	1.3844	1.3943	1.3930	1.3972	1.3937
$C_{16}-C_{17}$	1.385	1.3963	1.3973	1.3951	1.3831	1.3958	1.3941	1.3996	1.3948
$C_{17}-C_{12}$	1.404	1.4110	1.4121	1.4087	1.3977	1.4095	1.4078	1.4140	1.4083
RMSD		0.014	0.015	0.007	0.009	0.007	0.006	0.011	0.006
					Isolated Molecule				
C_1-C_2	1.539	1.5535	1.5571	1.5459	1.5463	1.5435	1.5428	1.5542	1.5456
C_2-C_3	1.531	1.5492	1.5524	1.5396	1.5319	1.5373	1.5368	1.5467	1.5393
C_3-C_4	1.524	1.5377	1.5403	1.5297	1.5202	1.5277	1.5270	1.5356	1.5293
C_4-C_5	1.521	1.5379	1.5403	1.5290	1.5232	1.5264	1.5262	1.5340	1.5287
C_5-C_6	1.533	1.5492	1.5525	1.5400	1.5317	1.5382	1.5369	1.5480	1.5396
C_6-C_1	1.540	1.5539	1.5571	1.5448	1.5459	1.5424	1.5419	1.5526	1.5445
C_1-N_1	1.560	1.6559	1.6693	1.6174	1.6094	1.6086	1.6084	1.6381	1.6168
N_1-C_7	1.506	1.5316	1.5343	1.5182	1.5104	1.5154	1.5152	1.5262	1.5179
C_7-C_8	1.520	1.5354	1.5387	1.5279	1.5201	1.5257	1.5247	1.5351	1.5276
C_8-C_9	1.522	1.5383	1.5412	1.5305	1.5230	1.5284	1.5276	1.5362	1.5302
C_9-C_{10}	1.517	1.5389	1.5416	1.5305	1.5229	1.5285	1.5273	1.5371	1.5303
$C_{10}-C_{11}$	1.520	1.5357	1.5390	1.5268	1.5203	1.5241	1.5238	1.5331	1.5265
$C_{11}-N_1$	1.512	1.5319	1.5345	1.5187	1.5093	1.5161	1.5156	1.5276	1.5183
C_1-C_{12}	1.536	1.5359	1.5394	1.5307	1.5295	1.5295	1.5277	1.5389	1.5304
$C_{12}-C_{13}$	1.398	1.4110	1.4137	1.4081	1.4033	1.4073	1.4059	1.4135	1.4079
$C_{13}-C_{14}$	1.393	1.3993	1.4013	1.3967	1.3921	1.3960	1.3947	1.4016	1.3965
$C_{14}-C_{15}$	1.384	1.3988	1.4005	1.3960	1.3915	1.3951	1.3939	1.3999	1.3958
$C_{15}-C_{16}$	1.378	1.3987	1.4005	1.3963	1.3914	1.3959	1.3943	1.4011	1.3961
$C_{16}-C_{17}$	1.385	1.3992	1.4012	1.3969	1.3924	1.3960	1.3948	1.4015	1.3965
$C_{17}-C_{12}$	1.404	1.4113	1.4138	1.4069	1.4053	1.4052	1.4046	1.4115	1.4067
RMSD		0.027	0.030	0.016	0.012	0.013	0.013	0.023	0.015

[a] For the atom labeling scheme, refer to Figure 2.

in fact, the average RMSD value is actually higher for the solid-state bond angles than for the isolated molecules. The majority of the deviation in the solid-state bond angles is due to the very poor reproduction of the bond angles by the HCTH functional. The RMSD values for the four best bond angle reproductions in the solid state are improved over their corresponding isolated-molecule values by an average of 13%.

b. Comparison of Experimental and Simulated THz Spectra. The cryogenic experimental THz spectrum is plotted along with the solid-state simulations in Figure 4. The simulations utilize the crystal cell parameters determined by the single crystal X-ray diffraction study included in this investigation. The figure is included to demonstrate the quality of fit with each of the eight GGA density functionals using the difference-dipole method. Each theoretical prediction is plotted both as a stick plot and as a convolved plot with an empirical Lorentzian line shape (3.0 cm^{-1} full width at half-maximum, fwhm).

A specific modification was made to each simulated spectrum. In all simulations, there was found to be one particular mode that had a significantly overestimated (by an order of magnitude over any peak in the experimental THz spectrum within several wavenumbers) intensity. In order to improve the fit to the experimental spectrum, the IR intensity of this mode has been set to zero in each simulation, leaving only the spectral intensity provided by the remaining 14 IR active modes present in the experimentally observed region. The removal of the intensity for this feature substantially improves the fit of the simulations. The analysis of this mode, identical in all eight density functionals, and additional consideration of the motion and the limit of the difference-dipole approximation as a useful model for describing this motion are provided in the Discussion. Other IR-active modes involving significant ion motions in the solid are combined with intramolecular vibrational components or combined ion/molecule motions which, taken as a whole in the difference-dipole calculation, result in far smaller changes in overall dipole magnitude in the mode and, therefore, much smaller calculated intensities.

Upon visual inspection, several of the simulations could be perceived as providing a reasonable reproduction of the experimental spectrum. A best performer has been determined

TABLE 3: [Functional]/DNP Solid State (PCP·HCl) and Isolated Molecule (PCP·H$^+$) Bond Angles (deg) and RMSD Values[a]

angle	exp	BLYP	BOP	BP	HCTH	PBE	PW91	RPBE	VWN-BP
				Solid State					
$C_1-C_2-C_3$	112.14	112.531	112.566	112.223	113.019	112.309	112.219	112.472	112.231
$C_2-C_3-C_4$	111.30	111.797	111.773	111.735	111.962	111.709	111.715	111.739	111.735
$C_3-C_4-C_5$	110.09	110.480	110.537	110.215	110.885	110.190	110.197	110.397	110.222
$C_4-C_5-C_6$	112.44	112.452	112.548	112.507	112.924	112.531	112.509	112.616	112.511
$C_5-C_6-C_1$	112.42	112.440	112.452	112.435	112.894	112.445	112.472	112.404	112.419
$C_6-C_1-C_2$	107.69	107.642	107.553	107.493	106.964	107.421	107.461	107.325	107.490
$C_6-C_1-N_1$	107.15	107.075	107.064	107.216	107.387	107.278	107.204	107.209	107.220
$C_2-C_1-N_1$	106.50	105.913	105.927	106.253	106.255	106.301	106.319	106.135	106.252
$C_1-N_1-C_7$	113.50	113.677	113.703	113.538	114.343	113.592	113.539	113.657	113.532
$N_1-C_7-C_8$	111.70	111.957	111.965	112.008	112.234	112.045	112.007	112.052	112.009
$C_7-C_8-C_9$	112.12	112.412	112.442	112.309	112.609	112.365	112.309	112.492	112.317
$C_8-C_9-C_{10}$	108.40	108.687	108.633	108.462	108.569	108.401	108.475	108.404	108.461
$C_9-C_{10}-C_{11}$	111.16	111.574	111.620	111.462	111.999	111.448	111.481	111.529	111.469
$C_{10}-C_{11}-N_1$	110.98	110.916	110.835	110.797	111.442	110.831	110.872	110.671	110.797
$C_{11}-N_1-C_1$	113.79	113.813	113.880	113.600	114.031	113.632	113.616	113.781	113.600
$N_1-C_1-C_{12}$	108.54	107.936	107.857	108.369	108.006	108.398	108.400	108.140	108.376
$C_6-C_1-C_{12}$	113.48	113.971	114.046	113.674	113.988	113.660	113.691	113.886	113.662
$C_2-C_1-C_{12}$	113.10	113.803	113.886	113.412	113.798	113.370	113.348	113.690	113.419
$C_1-C_{12}-C_{13}$	121.52	121.499	121.510	121.426	121.871	121.500	121.430	121.504	121.423
$C_{12}-C_{13}-C_{14}$	120.70	120.916	120.916	120.859	121.130	120.862	120.872	120.884	120.867
$C_{13}-C_{14}-C_{15}$	120.50	120.492	120.488	120.460	120.646	120.474	120.447	120.474	120.454
$C_{14}-C_{15}-C_{16}$	119.40	119.252	119.251	119.328	118.870	119.313	119.336	119.298	119.327
$C_{15}-C_{16}-C_{17}$	120.70	120.500	120.528	120.463	120.620	120.454	120.455	120.518	120.463
$C_{16}-C_{17}-C_{12}$	120.80	120.996	120.995	120.912	121.302	120.948	120.915	120.942	120.920
$C_{17}-C_{12}-C_1$	120.59	120.540	120.550	120.523	120.566	120.476	120.526	120.513	120.537
$C_7-N_1-C_{11}$	109.66	110.218	110.212	110.135	109.716	110.124	110.107	110.131	110.135
$C_{13}-C_{12}-C_{17}$	117.86	117.840	117.819	117.978	117.417	117.948	117.973	117.882	117.968
RMSD		0.328	0.351	0.205	0.519	0.205	0.195	0.287	0.206
				Isolated Molecule					
$C_1-C_2-C_3$	112.14	112.391	112.540	112.606	112.862	112.584	112.424	112.771	112.613
$C_2-C_3-C_4$	111.30	111.733	111.834	111.645	111.911	111.585	111.596	111.718	111.647
$C_3-C_4-C_5$	110.09	110.706	110.732	110.506	110.703	110.533	110.497	110.658	110.503
$C_4-C_5-C_6$	112.44	111.760	111.864	111.666	112.042	111.543	111.555	111.686	111.668
$C_5-C_6-C_1$	112.42	112.460	112.524	112.147	113.025	111.993	112.016	112.107	112.150
$C_6-C_1-C_2$	107.69	107.434	107.318	107.264	106.526	107.273	107.288	107.083	107.262
$C_6-C_1-N_1$	107.15	105.393	105.415	106.558	106.489	106.778	106.601	106.663	106.560
$C_2-C_1-N_1$	106.50	105.637	105.383	105.429	105.761	105.485	105.683	105.070	105.435
$C_1-N_1-C_7$	113.50	114.929	115.298	115.571	116.340	115.607	115.321	116.090	115.562
$N_1-C_7-C_8$	111.70	111.295	111.334	111.194	111.176	111.127	111.164	111.188	111.194
$C_7-C_8-C_9$	112.12	112.005	112.164	112.158	112.305	112.212	112.038	112.421	112.159
$C_8-C_9-C_{10}$	108.40	110.053	110.222	110.014	110.273	109.988	109.923	110.146	110.012
$C_9-C_{10}-C_{11}$	111.16	112.145	112.222	111.961	112.194	111.959	111.849	112.051	111.955
$C_{10}-C_{11}-N_1$	110.98	111.321	111.426	111.295	111.183	111.208	111.246	111.332	111.302
$C_{11}-N_1-C_1$	113.79	115.215	115.287	114.434	115.306	114.276	114.357	114.497	114.437
$N_1-C_1-C_{12}$	108.54	108.045	108.038	108.215	108.749	108.190	108.204	108.187	108.227
$C_6-C_1-C_{12}$	113.48	114.851	114.945	114.074	114.042	113.937	113.990	114.140	114.070
$C_2-C_1-C_{12}$	113.10	114.699	114.914	114.667	114.667	114.584	114.484	115.018	114.656
$C_1-C_{12}-C_{13}$	121.52	121.319	121.339	121.073	121.207	121.023	121.029	121.060	121.073
$C_{12}-C_{13}-C_{14}$	120.70	121.305	121.365	121.232	121.628	121.128	121.169	121.269	121.234
$C_{13}-C_{14}-C_{15}$	120.50	120.270	120.319	120.305	120.351	120.343	120.287	120.354	120.303
$C_{14}-C_{15}-C_{16}$	119.40	119.357	119.289	119.336	119.068	119.352	119.392	119.254	119.333
$C_{15}-C_{16}-C_{17}$	120.70	120.289	120.316	120.255	120.429	120.205	120.230	120.321	120.261
$C_{16}-C_{17}-C_{12}$	120.80	121.286	121.370	121.298	121.491	121.302	121.243	121.326	121.299
$C_{17}-C_{12}-C_1$	120.59	121.189	121.321	121.353	121.763	121.307	121.293	121.464	121.356
$C_7-N_1-C_{11}$	109.66	109.466	109.393	109.236	108.823	109.223	109.272	109.181	109.235
$C_{13}-C_{12}-C_{17}$	117.86	117.492	117.340	117.574	117.029	117.669	117.677	117.476	117.570
RMSD		0.265	0.293	0.241	0.312	0.236	0.219	0.285	0.241

[a] For the atom labeling scheme, refer to Figure 2.

by way of a two-step statistical analysis of first the residual spectral intensity and second the RMSD analysis of a selection of the predicted vibrational modes. Deviations in spectral intensity are determined by calculating the residual difference between the scaled best-fit intensity simulation for each functional and the cryogenic experimental spectrum. The resulting residual intensity RMSD values for the eight functionals are provided in Table 4, as are the RMSD values for the peak frequency deviations. On the basis of the residual intensity RMSD values determined by this method, the VWN-BP functional provides the most accurate simulation of spectral intensity.

The solid-state VWN-BP simulation predicts a total of 15 IR-active vibrational modes in the experimental range that are the basis for the eight features observed in the cryogenic experimental spectrum. Since the VWN-BP functional proved

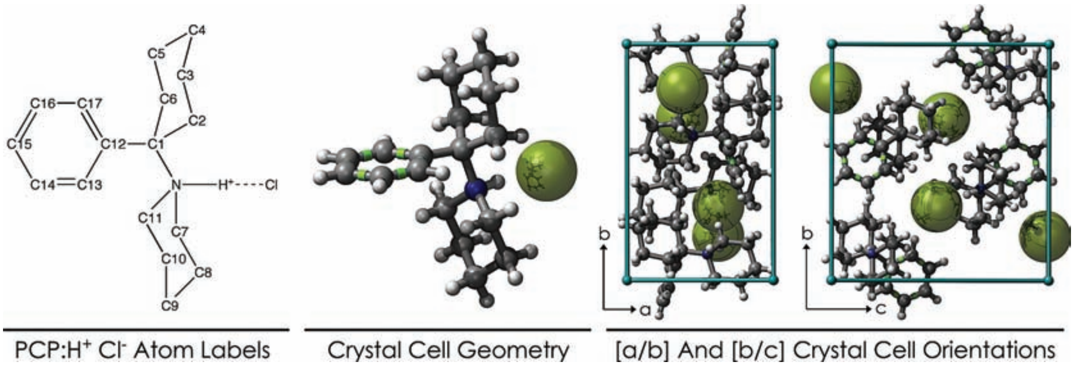

Figure 2. Phencyclidine molecule shown with the atomic labeling scheme (left), nearest crystal chlorine position (middle), and two views of the crystal unit cell of PCP•HCl. Figures rendered with NanoEngineer-1[41] and POV-Ray.[42]

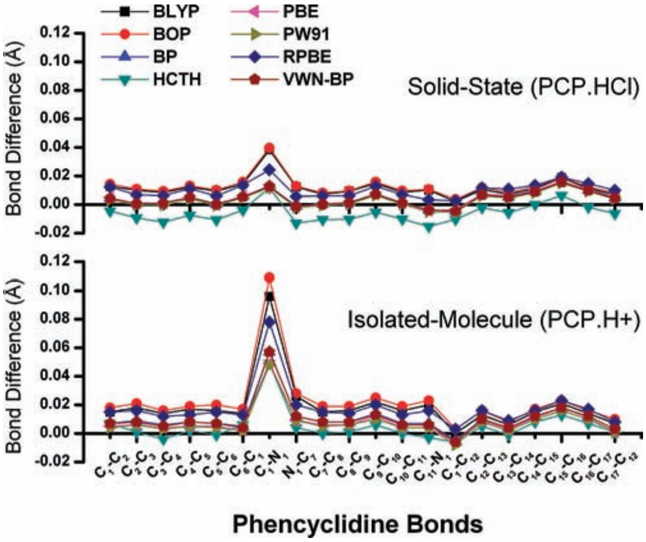

Figure 3. Differences in calculated bond lengths from experiment for the solid-state (PCP•HCl, top) and for the isolated-molecule (PCP•H$^+$, bottom) minimum-energy geometries.

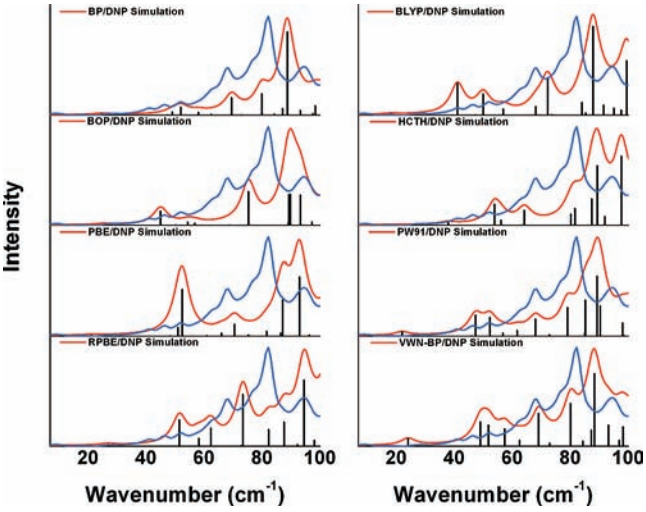

Figure 4. Comparison of the simulated and experimental (78.4 K) solid-state THz spectra of PCP•HCl from 7 to 100 cm^{-1}. The experimental spectrum is shown in blue. Black lines represent the calculated infrared intensity of each predicted mode. The red trace is a convolved plot of the theoretical vibrational modes using a 3.0 cm^{-1} (fwhm) Lorentzian line shape.

TABLE 4: Statistical Analysis of Quality-of-Fit to the Cryogenic Experimental THz Spectrum Obtained from DFT Simulations

exp	BLYP	BOP	BP	HCTH	PBE	PW91	RPBE	VWN-BP
				RMSD of Residual Intensity				
RMSD	0.244	0.283	0.265	0.273	0.283	0.222	0.207	0.187
				RMSD of Calculated Frequency for Six Correlated Vibrational Modes				
46.4	47.2	50.1	47.5	63.5	48.4	45.9	58.6	47.2
52.1	50.0	54.4	52.0	53.9	52.5	52.3	51.5	51.8
68.3	72.2	75.3	69.5	81.6	70.5	68.0	73.4	69.1
78.0	84.0	89.7	79.9	97.6	81.6	79.0	87.6	80.1
82.2	87.9	89.2	88.7	89.3	92.9	89.2	94.5	88.3
94.4	99.4	102.8	98.4	118.0	102.6	98.0	103.3	98.2
RMSD	4.4	7.4	3.3	15.6	5.8	3.2	9.1	3.1

most adept at the reproduction of spectral intensity, this calculation has been used as the reference from which to determine the capability of each of the GGA functionals to accurately predict the experimentally observed frequencies of PCP•HCl. This has been accomplished by assigning six predicted modes to the six experimentally observed peaks based upon calculated frequency and feature shape. The predicted assignments are made to the experimental absorptions occurring at 46.4, 52.1, 68.3, 78.0, 82.2, and 94.4 cm^{-1}. A corresponding motion was then identified in each of the seven remaining DFT simulations. In identification and assignment of the same motion from each of the eight simulations, a RMSD value can be determined for the calculated frequencies for each GGA functional. This approach would be expected to yield results biased toward the VWN-BP results based on the quality of fit of the most intense features and their contribution to the overall VWN-BP simulated line shapes, but it is worth stating for clarity that the agreement of individual features can be seen as distinct from the residual analysis, as the six pronounced features, the less-pronounced features, and their summation in the overall simulation account for more combined information to process than discrete mode assignments. In the absence of any experimental correlation, the peak RMSD values simply gauge how well individual functionals agree with one another on peak positions and their associated motions and not which is the best at reproducing experiment. By use of the results of the residual analysis as a starting point for the peak RMSD analysis, the best-fit residual functional becomes the basis for fixing the data set against experimental positions such that the individual mode correlations now occur against a proper reference data set (the cryogenic spectrum).

Table 4 provides the RMSD values for the peak positions for the eight functionals. Table 5 provides the vibrational frequencies predicted for all eight functionals by both solid-state and isolated-molecule methodologies. Overall, based upon both residual intensity and peak position, the VWN-BP functional is determined to provide a best-fit simulation of the

TABLE 5: The 15 Lowest-Frequency Solid State (PCP·HCl) and the Four Lowest Frequency Isolated Molecule (PCP·H^+) [Functional/DNP] Normal Modes (PCP·H^+ Intensities in km/mol)[a]

mode	BLYP	BOP	BP	HCTH	PBE	PW91	RPBE	VWN-BP
a	**18.3**	**25.1**	**24.7**	**37.9**	**21.2**	**22.0**	**26.9**	**24.1**
b	**41.1**	**45.0**	**47.5**	**53.9**	**48.4**	**45.9**	**51.5**	**47.2**
c	**47.2**	**50.1**	**49.1**	**56.1**	**51.0**	**47.3**	**58.2**	**49.0**
d	**50.0**	**54.4**	**52.0**	**63.5**	**52.5**	**52.3**	**58.6**	**51.8**
e	**56.9**	**56.8**	**58.0**	**64.2**	**61.0**	**56.8**	**62.3**	**57.4**
f	**68.1**	**68.7**	**62.5**	**80.2**	**66.0**	**61.7**	**72.7**	**62.5**
g	**72.2**	**75.3**	**69.5**	**81.6**	**70.5**	**68.0**	**73.4**	**69.1**
h	**73.6**	**75.7**	**73.0**	**87.4**	**75.3**	**72.8**	**82.3**	**72.9**
i	**84.0**	**89.1**	**79.9**	**89.3**	**81.6**	**79.0**	**87.6**	**80.1**
j	**85.3**	**89.2**	**84.2**	**91.9**	**86.4**	**85.0**	**92.2**	**84.3**
k	**87.8**	**89.7**	**87.1**	**97.6**	**87.1**	**85.2**	**94.5**	**87.2**
l	**91.5**	**93.2**	**88.7**	102.4	**92.9**	**89.2**	**98.0**	**88.3**
m	**95.0**	**97.2**	**93.2**	110.0	**96.3**	**90.3**	103.3	**93.1**
n	**97.5**	101.4	**97.5**	117.6	101.7	**98.0**	107.1	**96.9**
o	**99.4**	102.8	**98.4**	118.0	102.6	**98.6**	108.2	**98.2**
1	**20.4** (0.00)	**9.4** (0.00)	**37.2** (0.00)	**76.0** (0.17)	**24.6** (0.01)	**25.4** (0.00)	**64.9** (0.09)	**37.0** (0.00)
2	**58.0** (0.13)	**58.4** (0.13)	**61.0** (0.13)	**92.1** (0.03)	**56.9** (0.16)	**54.1** (0.12)	**72.2** (0.07)	**60.8** (0.13)
3	**67.1** (0.01)	**63.2** (0.01)	**76.5** (0.05)	100.3 (0.02)	**76.7** (0.04)	**69.5** (0.07)	**90.0** (0.06)	**76.1** (0.05)
4	**78.1** (0.16)	**79.5** (0.17)	**83.3** (0.14)	128.3 (0.20)	**90.5** (0.13)	**74.7** (0.17)	109.7 (0.12)	**83.0** (0.14)

[a] The calculated IR intensity is included for the isolated-molecule normal modes. Modes within the measured region (below ~100 cm^{-1}) are shown in boldface.

experimental spectrum, which is to say that the major components responsible for much of the structure of the VWN-BP line shape are in close proximity to discernible peaks in the cryogenic spectrum. The correlation analysis reveals that the VWN-BP, PW91, and BP density functionals are in remarkably good agreement with one another, with this narrow spread indicating that these three functionals strongly agree with each other in a particular spectral peak corresponding to the same normal mode.

The PW91 simulation provides the third-best RMSD value in terms of residual intensity and the second-best RMSD value in terms of peak frequency. The BLYP and BP functionals also provide acceptable simulations of the solid-state THz experiment. The BLYP simulation provides the fourth-best residual intensity and peak frequency RMSD value, while the BP simulation provides the fifth-best residual intensity RMSD value and the third-best RMSD value for peak frequency. The ability of these four different functionals to all provide reasonably good simulations of the experimental spectrum reiterates the potential for multiple functionals to accurately replicate experimental solid-state THz spectra.

While there is overall line shape agreement among several of the functionals, significant deviations are certainly visible when the data set is taken as a whole. Part of the difference between the simulations is based on the different numbers of vibrational modes predicted to occur *in the experimental range* by each functional. The number of predicted modes differs from as few as 11 for the HCTH functional to as many as 15 modes predicted by four different functionals (BLYP, BP, PW91, VWN-BP) below 100 cm^{-1}. The empirical derivation of density functionals means, as is obvious from the normal mode analyses performed here, that differing formulations can produce significantly different answers in terms of structural parameters, number of modes predicted within an experimental range, and vibrational frequencies. The differences between the functionals lead to the strong possibility that a mode predicted to occur in the experimental range by one functional could be shifted well outside of the experimental range by another functional. This point is all the more relevant to the presented analysis given the narrow range of the experimental spectrum (and the similarly narrow range reported in many THz studies).

c. THz Mode Assignments Based Upon the VWN-BP/DNP Simulated Spectrum. On comparison of the DFT simulations, the VWN-BP solid-state spectrum delivers the best agreement with the experimental cryogenic spectrum in terms of both spectral intensity and peak position. The VWN-BP simulation is therefore utilized to assign the vibrations that comprise the experimental spectral features. Assignment of the absorptions included in the cryogenic spectrum is performed by using the frequency analyses provided by both the isolated-molecule and the solid-state simulations. The isolated-molecule calculations are used in order to identify and assign internal modes present in the solid-state calculations.

A crystal unit cell containing M molecules with N atoms contains $3N - 6M$ internal modes (those modes associated with intramolecular motions), $6M - 3$ external modes (those modes associated with relative motions between the M molecules, such as rotations and translations), and three acoustic modes. The crystal cell of PCP·HCl includes four molecules ($Z = 4$); each asymmetric unit contains 180 atoms. PCP·HCl includes a total of 21 external vibrational modes and 516 internal vibrations.

The identity and description of the labeled vibrational modes established from the VWN-BP simulation are provided in Table 6. The labeling scheme for the mode assignments provided in Table 6 is provided in Figure 5, with the net motions of molecules within the reference frame of the unit cell assigned as *in-phase* and *out-of-phase* based on the labeled (and colorized) arrangement. The solid-state vibrations contained in PCP·HCl are generally assignable as internal (molecular bending and torsions) or as external modes (translations and rotations). Some of the predicted modes exhibit both internal and external character, a result that has been seen in earlier investigations of similar compounds.[36,40] Assignment of the 15 VWN-BP modes contained within the experimental frequency range is made based upon the most substantial contributor to the character of the mode when one contributor is clearly dominant. The vibrational modes present in the experimental cryogenic THz spectrum of solid-state PCP·HCl are labeled in Figure 6 as modes a through o. The range of calculated intensities across these 15 modes is quite large. The calculated intensity of the most intense mode (l) is nearly 27 times more intense than the calculated intensity of the least intense mode

TABLE 6: Vibrational Mode Assignments of PCP·HCl at the VWN-BP/DNP Level of Theory[a]

mode	cm^{-1}	mode description[b]	% of total intensity
		Solid State	
a	24.1	OT along crystal *a* axis, (A + C) − (B + D)	2.60
b	47.2	OR along crystal *a* axis, (A + D) − (B + C)	0.00
c	49.0	37.0, (A + B) − (C + D)	8.23
d	51.8	OT along crystal *c* axis, (A + C) − (B + D)	7.11
e	57.4	OR along crystal *c* axis, (A + B) − (C + D)	5.92
f	62.5	83.0, (A + D) − (B + C)	1.94
g	69.1	OR along crystal *b* axis, (A + D) − (B + C)	11.14
h	72.9	OR along crystal *b* axis, (A + B) − (C + D)	0.93
i	80.1	37.0 + OT along crystal *b* axis, (A + B) - (C + D)	14.53
j	84.3	60.8, (A + B) − (C + D) + Cl$^-$ translation	1.63
k	87.2	60.8, (A + B) − (C + D)	5.44
l	88.3	83.0, (A + B) − (C + D) + Cl$^-$ translation	24.82
m	93.1	76.1, (A + D) − (B + C)	7.17
n	96.9	76.1 + Cl$^-$ OT along crystal *b* axis	1.99
o	98.2	83.0 + Cl$^-$ OT along crystal *b* axis, (A + B) − (C + D)	6.54
		Isolated-Molecule Motions	
1	37.0	N_1-C_1 torsional mode	
2	60.8	$N_1-C_1-C_{12}$ bending mode	
3	76.1	N_1-C_1, C_1-C_{12} torsion in-phase + phenyl rotation	
4	83.0	N_1-C_1, C_1-C_{12} torsion out-of-phase + phenyl rotation	

[a] See Figure 6 for molecule labels and combination/phase description. [b] Key: OR = optical rotation, OT = optical translation.

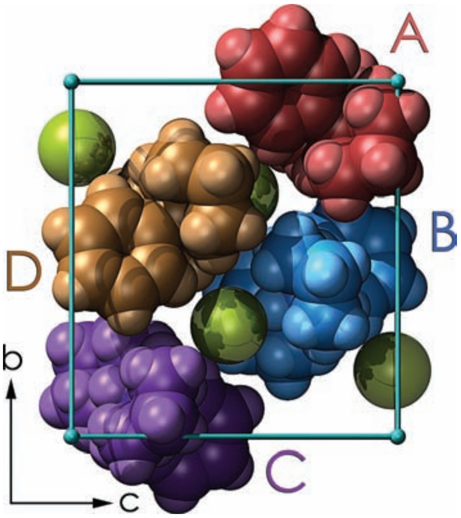

Figure 5. Labeling scheme used for the description of internal and external vibrational mode combinations in Table 6. Cell contents move in (+) or out of phase (−) with respect to each other in the reference frame of the crystal cell. See text.

(h). The chloride anions are not differentiated by color in Figure 5 because their predicted motions in the VWN-BP calculations are always in-phase with respect to one another (so translational Cl$^-$ motions in THz-active modes always move in the same direction and, therefore, do not require labeled associations with individual PCP molecules).

A plot of the vibrational modes predicted by the VWN-BP based isolated-molecule calculation within the experimental range is included as Figure 7 in order to demonstrate the substantial failure of the isolated-molecule calculation in providing an accurate model of the two experimental THz spectra. This plot clearly shows the inability of the isolated-molecule calculation to fit the experimental spectrum, as only four modes are predicted by the isolated-molecule calculations despite the presence of eight experimental features in the cryogenic spectrum. This point is emphasized here because the use of isolated-molecule calculations for solid-state THz assignments is still a method employed even in recent THz studies despite an increasing wealth of published examples that clearly address the importance of the treatment of solid-state samples by solid-state theoretical methods.

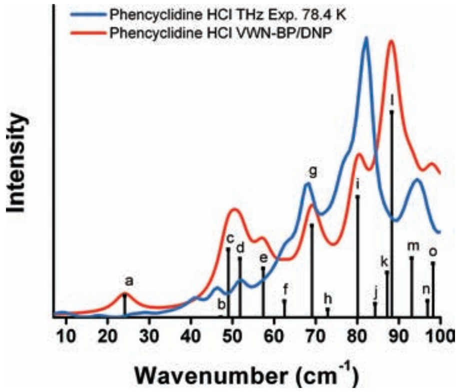

Figure 6. Comparison of the VWN-BP/DNP and cryogenic solid-state THz spectra for PCP·HCl. The experiment is shown in blue. The infrared intensity of the modes predicted using the VWN-BP density functional is shown as black lines. The red trace is a convolved plot of the predicted modes using a 3.0 cm^{-1} Lorentzian line shape. Mode labels are detailed in Table 6.

IV. Discussion

The cryogenic THz spectrum of PCP·HCl reveals several low intensity features that are not visible in the RT spectrum. This improved resolution enables a more complete and detailed characterization of the low-energy vibrational structure of this crystalline compound. The improved resolution afforded by cryogenic measurements aids in the validation of theoretical modeling techniques and substantially simplifies the assignment of experimental THz features.

To assign the experimental spectrum of a molecular solid, only solid-state methods are appropriate. The isolated-molecule approach neglects intermolecular interactions that define both molecular conformations and changes to functional groups arising from electrostatic phenomena, as well as neglects the external vibrational modes that are the result of molecules existing in defined sites in a lattice and undergoing motions with respect to one another in the crystal cell. In the case of PCP·HCl, the solid-state calculations predict the presence of 15 IR-active modes in the experimental range, while the isolated-molecule calculations predict no more than four modes. The disparity in the number of predicted modes between solid-state and isolated-molecule calculations speaks directly to the need

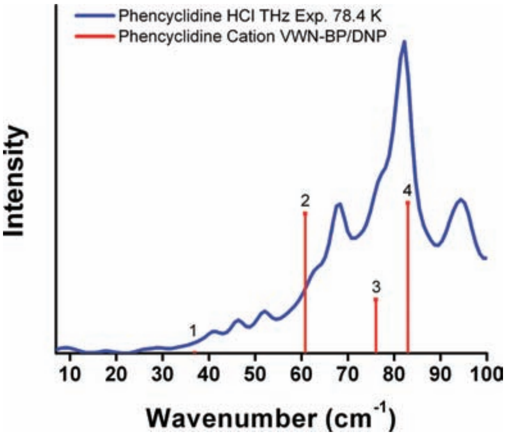

Figure 7. Comparison of the experimental solid-state THz spectrum of PCP·HCl to the vibrational modes predicted by the VWN-BP/DNP isolated-molecule calculation. The experimental spectrum is shown in blue. The infrared intensity of the predicted modes is shown as red lines.

for the incorporation of crystal cell contents and their interactions to properly predict vibrational spectra. The neglect of these interactions is irrefutably an error when trying to simulate solid-state THz spectra.

The consideration of the crystal cell for the simulation of THz spectra and other solid-state phenomena in molecular solids has become increasingly practical with both the development of solid-state DFT codes capable of treating these systems at sufficiently high levels of theory and computational resources capable of completing these larger calculations (relative to the isolated-molecule calculations that served as the basis of much spectroscopic assignment in THz spectroscopy previously). The difference-dipole method for the calculation of intensities in the solid state, an approximation required in DMol^3 because this functionality is not available in the code, has proven useful in several previous studies of neutral molecular solids where changes to atomic charge as a function of displacement along a normal coordinate are not themselves large. In ionic solids, both the magnitude of the eigenvector for an atomic displacement and the treatment of the charge separation between anion and cation are factors that must be described very accurately in order for there to be reasonable correspondence between the magnitude of internal and external vibrational mode dipole moments. In the PCP·HCl difference-dipole calculation, the mode for which the calculated intensity was ignored in the spectral simulation is that of an optical rotation along the crystal *a* axis that includes some small quantity of $N-H^+\cdots Cl^-$ stretching. This mode is unique among all other IR-active external modes because the molecular combination involved in the motion has all $N-H^+\cdots Cl^-$ charge pairs rotating (and slightly stretching) as to produce one massive net change in dipole along the crystal *a* axis. While it would have been just as easy to apply a scalar to this mode to compensate for this large *a* axis dipole difference between the ground and mode-displaced mode or to displace along the normal coordinate only to the point where the difference-dipole approximation provided an intensity value in correspondence with experiment, the good agreement in, for instance, the VWN-BP simulation for all other modes means that no single approach that corrected this *a* axis optical rotation intensity would be applicable for improving agreement between theory and experiment. It is clear that, if the difference-dipole approach is to serve as useful in either quantum chemical or molecular dynamics based THz simulations, a much larger sampling of ionic systems and treatment of ionic interactions is needed.

It is shown that the VWN-BP simulation provides the best-fit reproduction of the experimental spectrum. Certainly, deviations can be noted in terms of both spectral intensity and absorption frequency, but in general the fit to the experiment is quite good. The most noticeable deviation from the experimental spectrum by the simulation is the overestimation of the intensity of modes b, c, and d. As has been noted earlier in the paper, the intensity of mode b was substantially overestimated and its intensity has been set to zero in the plot. Additionally, it appears the predicted frequencies of modes b and c are slightly overcalculated. The predicted intensity of mode a is questionable because no feature is distinguishable in this region of the experimental spectrum. In terms of frequency, more deviations are present as both modes i and l appear to be overcalculated by several wavenumbers. The overestimation of many of the predicted mode frequencies is the reason for which mode o, which occurs at 98.2 cm^{-1}, rather than mode m, has been assigned to the experimental feature occurring at 94.4 cm^{-1}. The overcalculation of several of the predicted modes leads to the belief that mode m has also likely been overestimated, therefore this mode is believed to provide the slight shouldering effect seen in the experimental spectrum at roughly 88 cm^{-1}.

The VWN-BP simulation provides the best spectral simulation, but it is important to note that other simulations do provide reasonable predictions. The PW91 simulation is one example, as it provides a good spectral simulation and reproduces the structural geometry as accurately as the VWN-BP prediction. The ability of the PW91 functional to simultaneously predict experimental THz spectra and molecular structure accurately has been highlighted in earlier work on the methamphetamine and ephedrine molecules.[36,40] The differing formulations present in each functional will inherently lead to differences between the calculated outputs and the resulting simulations. The differences between simulations indicate that, as methodologies continue to undergo improvements, certain density functionals will continue to be utilized for THz modeling, while others will be deemed incapable of treating low-lying internal vibrations and intermolecular/crystal packing interactions and not be utilized. A goal of this work is to further highlight the differences between individual density functionals in their ability to accurately and reliably simulate THz spectra.

In an attempt to provide the best possible simulation of the experimental spectrum in the THz region, the use of a frequency scale factor was tested as a way to increase the quality of fit of the theoretical VWN-BP/DNP simulated solid-state spectrum. A series of scale factors were tested and, based upon minimization of residual intensity, a factor of 0.95 applied to the calculated frequencies was found to minimize the residual intensity. Figure 8 depicts the scaled VWN-BP simulation plotted against the cryogenic experimental spectrum for PCP·HCl. The calculated residual intensity RMSD decreased to 0.142, a decrease of 24% over the calculated residual intensity value provided by the nonscaled simulation. Additionally, by applying the frequency scale factor to the simulation, the RMSD value determined for the peak frequencies was also substantially improved, as the calculated frequency RMSD decreased by a third, from 3.1 to 2.1. To date, theoretical frequency scale factors for the far-infrared region have not been established. However, these data indicate that the use of the scale factors may be quite beneficial in the precise simulation of experimental THz spectra.

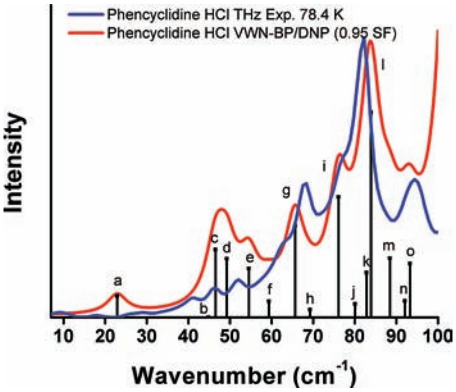

Figure 8. Comparison of the scaled VWN-BP/DNP and cryogenic solid-state THz spectra for PCP·HCl. The theoretical simulation is plotted using a 0.95 scale factor (SF). The experiment is shown in blue. The infrared intensity of the modes predicted using the VWN-BP density functional is shown as black lines. The red trace is a convolved plot of the predicted modes using a 3.0 cm^{-1} Lorentzian line shape.

V. Conclusions

THz vibrational spectra of phencyclidine hydrochloride at room and liquid-nitrogen temperatures have been measured from 7.0 to 100.0 cm^{-1} and have been assigned utilizing solid-state DFT calculations. The cryogenic investigation uncovers low intensity features not discernible in the room temperature study. The solid-state calculations, by accounting for crystal cell interactions, provide accurate reproductions of the solid-state compound structural parameters and enable the creation of excellent simulations of the experimentally observed cryogenic THz spectrum. Assignment of the spectral absorptions has been performed based upon the vibrational frequencies and infrared intensities provided by solid-state normal mode analyses utilizing the VWN-BP functional combined with the DNP basis set. The theoretical analysis suggests the basis of the eight features found in the experimental spectrum is a total of 15 IR-active vibrational modes. A large portion of the observed spectral intensity, approximately 42%, is derived from external vibrational modes. Isolated-molecule calculations are insufficient for the spectral reproduction of the title compound, as the presence of no more than four vibrational modes is predicted in the experimental range of this study by that approach. This investigation further demonstrates the ability of solid-state DFT to assist in the accurate reproduction of experimental solid-state THz spectra and demonstrates the necessity of the inclusion of crystal packing interactions to accurately simulate and understand the THz spectra of molecular solids.

Acknowledgment. This work was supported by a grant from the National Science Foundation CAREER Program (CHE-0847405). This work was partially supported by the National Center for Supercomputing Applications under [TG-CHE080041N] and utilized the SGI Altix [Cobalt]. P.M.H. expresses his gratitude to the Syracuse University STEM and GEM Fellowship programs for their continued support. D.G.A. thanks the office of the Vice President for Research at Syracuse University for research support. The authors also acknowledge Dr. John M. Belote (Syracuse University) for his assistance in procuring the research samples.

Supporting Information Available: Atomic positional parameters, full tables of bond lengths and angles, and anisotropic temperature factors are available. This material is available free of charge via the Internet at http://pubs.acs.org.

References and Notes

(1) Hu, Y.; Huang, P.; Guo, L.; Wang, X.; Zhang, C. *Phys. Lett. A* **2006**, *359*, 728.

(2) Leahy-Hoppa, M. R.; Fitch, M. J.; Zheng, X.; Hayden, L. M.; Osiander, R. *Chem. Phys. Lett.* **2007**, *434*, 227.

(3) Federici, J. F.; Schulkin, B.; Huang, F.; Gary, D.; Barat, R.; Oliveira, F.; Zimdars, D. *Semicond. Sci. Technol.* **2005**, *20*, S266.

(4) Taday, P. F. *Philos. Trans. R. Soc. London, Ser. A* **2004**, *362*, 351.

(5) Zeitler, J. A.; Taday, P. F.; Newnham, D. A.; Pepper, M.; Gordon, K. C.; Rades, T. *J. Pharm. Pharmacol.* **2007**, *59*, 209.

(6) Wang, G.; Shen, J.; Jia, Y. *J. Appl. Phys.* **2007**, *102*, 013106/1.

(7) Dobroiu, A.; Sasaki, Y.; Shibuya, T.; Otani, C.; Kawase, K. *Proc. IEEE* **2007**, *95*, 1566.

(8) Lu, M.; Shen, J.; Li, N.; Zhang, Y.; Zhang, C.; Liang, L.; Xu, X. *J. Appl. Phys.* **2006**, *100*, 103104/1.

(9) *Principles of Forensic Toxicology*, 2nd ed.; Levine, B., Ed.; AACC Press: Washington, DC, 2003.

(10) Nahata, A.; Weling, A. S.; Heinz, T. F. *Appl. Phys. Lett.* **1996**, *69*, 2321.

(11) Rice, A.; Jin, Y.; Ma, X. F.; Zhang, X. C.; Bliss, D.; Larkin, J.; Alexander, M. *Appl. Phys. Lett.* **1994**, *64*, 1324.

(12) Wu, Q.; Litz, M.; Zhang, X. C. *Appl. Phys. Lett.* **1996**, *68*, 2924.

(13) Johnson, K. W.; Rabolt, J. F. *J. Chem. Phys.* **1973**, *58*, 4536.

(14) Chantry, G. W.; Fleming, J. W.; Nicol, E. A.; Willis, H. A.; Cudby, M. E. A. *Chem. Phys. Lett.* **1972**, *16*, 141.

(15) Duvillaret, L.; Garet, F.; Coutaz, J.-L. *IEEE J. Sel. Top. Quantum Electron.* **1996**, *2*, 739.

(16) Bruker, A. *SMART Software, 5.630 ed.*; Siemens Analytical X-ray Instruments, Inc.: Madison, WI, 1994.

(17) Sheldrick, G. M. *SADABS: Program for Empirical Absorption Corrections*; University of Gottingen: Gottingen, Germany, 1996.

(18) *International Tables for Crystallography, Vol. C: Mathematical, physical and chemical tables*; Springer: Berlin, 2006.

(19) Sheldrick, G. M. *SHELXTL-Plus: Program for Refinement of Crystal Structures, 6.14 ed.*; Madison, WI, 1996.

(20) Sheldrick, G. M. *SAINT-Plus, 6.45 ed.*; Bruker-AXS: Madison, WI, 1996.

(21) Argos, P.; Barr, R. E.; Weber, A. H. *Acta Crystallogr., Sect. B: Struct. Sci.* **1970**, *26*, 53.

(22) Delley, B. *J. Chem. Phys.* **1990**, *92*, 508.

(23) Delley, B. *J. Chem. Phys.* **2000**, *113*, 7756.

(24) Becke, A. D. *Phys. Rev. A: At., Mol., Opt. Phys.* **1988**, *38*, 3098.

(25) Lee, C.; Yang, W.; Parr, R. G. *Phys. Rev. B: Condens. Matter Mater. Phys.* **1988**, *37*, 785.

(26) Tsuneda, T.; Suzumura, T.; Hirao, K. *J. Chem. Phys.* **1999**, *110*, 10664.

(27) Perdew, J. P.; Chevary, J. A.; Vosko, S. H.; Jackson, K. A.; Pederson, M. R.; Singh, D. J.; Fiolhais, C. *Phys. Rev. B: Condens. Matter Mater. Phys.* **1992**, *46*, 6671.

(28) Boese, A. D.; Handy, N. C. *J. Chem. Phys.* **2001**, *114*, 5497.

(29) Perdew, J. P.; Yue, W. *Phys. Rev. B: Condens. Matter Mater. Phys.* **1986**, *33*, 8800.

(30) Perdew, J. P.; Burke, K.; Ernzerhof, M. *Phys. Rev. Lett.* **1996**, *77*, 3865.

(31) Perdew, J. P.; Burke, K.; Ernzerhof, M. *Phys. Rev. Lett.* **1997**, *78*, 1396.

(32) Hammer, B.; Hansen, L. B.; Norskov, J. K. *Phys. Rev. B: Condens. Matter Mater. Phys.* **1999**, *59*, 7413.

(33) Vosko, S. H.; Wilk, L.; Nusair, M. *Can. J. Phys.* **1980**, *58*, 1200.

(34) Allis, D. G.; Korter, T. M. *ChemPhysChem* **2006**, *7*, 2398.

(35) Allis, D. G.; Prokhorova, D. A.; Korter, T. M. *J. Phys. Chem. A* **2006**, *110*, 1951.

(36) Hakey, P. M.; Allis, D. G.; Ouellette, W.; Korter, T. M. *J. Phys. Chem. A* **2009**, *113*, 5119.

(37) Franzen, S. *J. Phys. Chem. A* **2003**, *107*, 9898.

(38) Laman, N.; Harsha, S. S.; Grischkowsky, D.; Melinger, J. S. *Opt. Express* **2008**, *16*, 4094.

(39) Walther, M.; Plochocka, P.; Fischer, B.; Helm, H.; Jepsen, P. U. *Biopolymers* **2002**, *61*, 310.

(40) Hakey, P. M.; Allis, D. G.; Hudson, M. R.; Ouellette, W.; Korter, T. M. *ChemPhysChem*, in press.

(41) *NanoEngineer-1, v1.1.0*; Nanorex Inc., Bloomfield Hill, MI, 2007, www.nanorex.com.

(42) *POV-Ray, Persistence of Vision Raytrace Program, v3.6*; www.povray.org.

JP907083U